Spectroscopic evidence for bulk-band inversion and three-dimensional massive Dirac fermions in $ZrTe_5$

Zhi-Guo Chen (谌志国)[a,1], R. Y. Chen[b], R. D. Zhong[c], John Schneeloch[c], C. Zhang[c], Y. Huang[d], Fanming Qu[a,e], Rui Yu[f], Q. Li[c], G. D. Gu[c], and N. L. Wang[b,g,1]

[a]Beijing National Laboratory for Condensed Matter Physics and Institute of Physics, Chinese Academy of Sciences, Beijing 100190, China; [b]International Center for Quantum Materials, School of Physics, Peking University, Beijing 100871, China; [c]Condensed Matter Physics and Materials Science Department, Brookhaven National Lab, Upton, NY 11973; [d]Center for Functional Nanomaterials, Brookhaven National Lab, Upton, NY 11973; [e]QuTech, Delft University of Technology, Delft, 2600 GA, The Netherlands; [f]School of Physics and Technology, Wuhan University, Wuhan 430072, China; and [g]Collaborative Innovation Center of Quantum Matter, Beijing 100871, China

Edited by J. C. Séamus Davis, Cornell University, Ithaca, NY, and approved December 13, 2016 (received for review August 7, 2016)

Three-dimensional topological insulators (3D TIs) represent states of quantum matters in which surface states are protected by time-reversal symmetry and an inversion occurs between bulk conduction and valence bands. However, the bulk-band inversion, which is intimately tied to the topologically nontrivial nature of 3D Tis, has rarely been investigated by experiments. Besides, 3D massive Dirac fermions with nearly linear band dispersions were seldom observed in TIs. Recently, a van der Waals crystal, $ZrTe_5$, was theoretically predicted to be a TI. Here, we report an infrared transmission study of a high-mobility [~33,000 $cm^2/(V \cdot s)$] multilayer $ZrTe_5$ flake at magnetic fields (B) up to 35 T. Our observation of a linear relationship between the zero-magnetic-field optical absorption and the photon energy, a bandgap of ~10 meV and a $\sqrt{B}$ dependence of the Landau level (LL) transition energies at low magnetic fields demonstrates 3D massive Dirac fermions with nearly linear band dispersions in this system. More importantly, the reemergence of the intra-LL transitions at magnetic fields higher than 17 T reveals the energy cross between the two zeroth LLs, which reflects the inversion between the bulk conduction and valence bands. Our results not only provide spectroscopic evidence for the TI state in $ZrTe_5$ but also open up a new avenue for fundamental studies of Dirac fermions in van der Waals materials.

band inversion | Dirac fermions | topological insulators | Landau levels | Zeeman splitting

Topologically nontrivial quantum matters, such as topological insulators (1–8), Dirac semimetals (9–19), and Weyl semimetals (20–27), have sparked enormous interest owing both to their exotic electronic properties and potential applications in spintronic devices and quantum computing. Therein, intrinsic topological insulators have insulating bulk states with odd Z_2 topological invariants and metallic surface or edge states protected by time-reversal symmetry (4–6, 28). Most of the experimental evidence to date for TIs is provided by the measurements of the spin texture of the metallic surface states. As a hallmark of the nontrivial Z_2 topology of TIs (4–6, 28), an inversion between the characteristics of the bulk conduction and valence bands occurring at an odd number of time-reversal invariant momenta has seldom been probed by experiments. An effective approach for identifying the bulk-band inversion in TIs is to follow the evolution of two zeroth Landau levels (LLs) that arise from the bulk conduction and valence bands, respectively. As shown in Fig. 1*A*, for TIs, due to the bulk-band inversion and Zeeman effects, the two zeroth bulk Landau levels are expected to intersect in a critical magnetic field and then separate (3, 29); and for trivial insulators, the energy difference between their two zeroth Landau levels would become larger with increasing magnetic field. Therefore, an intersection between the two zeroth bulk LLs is a significant signature of the bulk-band inversion in TIs. However, a spectroscopic study of the intersection between the two zeroth bulk LLs in 3D TIs is still missing. In addition, many typical 3D TIs, such as Bi_2Se_3, show massive bulk Dirac fermions with parabolic band dispersions, which are effectively described by massive Dirac models (6, 28, 29). By contrast, 3D massive Dirac fermions with nearly linear bulk band dispersions (7), which are interesting topics following 2D massive Dirac fermions in gapped graphene (30, 31), were rarely observed in 3D TIs.

A transition-metal pentatelluride, $ZrTe_5$, embodies both 1D chain and 2D layer features (32), shown in Fig. 1*B*. One Zr atom together with three Te (1) atoms forms a quasi-1D prismatic chain $ZrTe_3$ along the a axis (x axis). These prismatic $ZrTe_3$ chains are connected through zig-zag chains of Te (2) atoms along the c axis (y axis) and then construct quasi-2D $ZrTe_5$ layers. The bonding between $ZrTe_5$ layers is van der Waals type (33, 34). Thus, as displayed in Fig. 1*C*, bulk $ZrTe_5$ crystals can be easily cleaved down to a few layers. Recently, the ab initio calculations indicate that monolayer $ZrTe_5$ sheets are great contenders for quantum spin Hall insulators—2D TI and that 3D $ZrTe_5$ crystals are quite close to the phase boundary between strong and weak TIs (33). Scanning tunneling microscopy measurements have shown that edge states exist at the step edges of the $ZrTe_5$ surfaces (35, 36). Nonetheless, further investigations are needed to check whether the observed edge states in $ZrTe_5$ are topologically nontrivial or not. Studying the bulk-band inversion or the intersection between the two zeroth bulk LLs can provide a crucial clue to clarifying the nature of the edge states in $ZrTe_5$. Except the edge states within the energy gap of the bulk bands around the Brillouin zone center (i.e., Γ point) of $ZrTe_5$ (36, 37), 3D massless Dirac fermions with

Significance

Experimental verifications of the theoretically predicted topological insulators (TIs) are essential steps toward the applications of the topological quantum phenomena. In the past, theoretically predicted TIs were mostly verified by the measurements of the topological surface states. However, as another key feature of the nontrivial topology in TIs, an inversion between the bulk bands has rarely been observed by experiments. Here, by studying the optical transitions between the bulk LLs of $ZrTe_5$, we not only offer spectroscopic evidence for the bulk-band inversion—the crossing of the two zeroth LLs in a magnetic field, but also quantitatively demonstrate three-dimensional massive Dirac fermions with nearly linear band dispersions in $ZrTe_5$. Our investigation provides a paradigm for identifying TI states in candidate materials.

Author contributions: Z.-G.C. designed the research; Z.-G.C. carried out the optical experiments; Z.-G.C. wrote the paper; Z.-G.C., R.Y.C., R.Y., and N.L.W. analyzed the data; R.D.Z., J.S., and G.D.G. grew the single crystals; and C.Z., Y.H., F.Q., and Q.L. performed the basic characterization.

The authors declare no conflict of interest.

This article is a PNAS Direct Submission.

[1]To whom correspondence may be addressed. Email: zgchen@iphy.ac.cn or nlwang@pku.edu.cn.

This article contains supporting information online at www.pnas.org/lookup/suppl/doi:10.1073/pnas.1613110114/-/DCSupplemental.

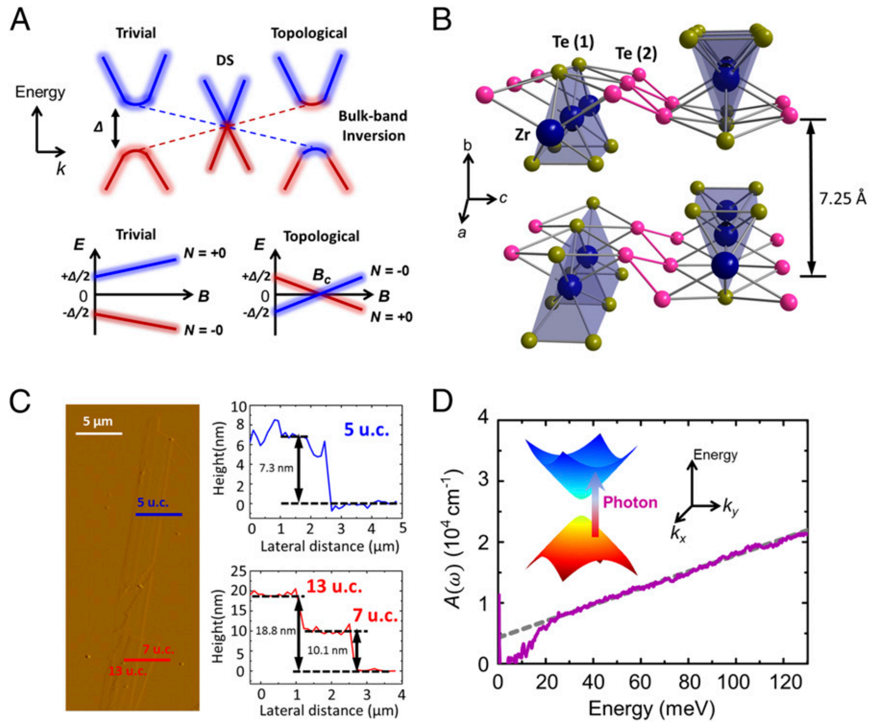

Fig. 1. Bulk band and crystal structure of $ZrTe_5$. (*A, Top*) Schematic of the topological phase transition from trivial to topological insulators. A 3D Dirac semimetal (DS) can be regarded as a quantum critical point with a gapless band structure. Due to the bulk-band inversion in TIs, the conduction and valence band exchange their extrema. Bottom row: energy spectrum for the Landau-index $N = +0$ and -0 LLs with a Zeeman splitting. (*B*) Atomic structure of $ZrTe_5$. Each unit cell contains two $ZrTe_5$ layers. (*C, Left*) AFM image of $ZrTe_5$ flakes. (*Right*) thicknesses along the colored lines on the left. Thicknesses from 5 to 13 unit cells (u.c.) are shown. (*D*) Absorption coefficient $A(\omega)$ of the $ZrTe_5$ flake with thickness d ~180 nm as a function of photon energy at $B = 0$ T. The linear energy dependence of $A(\omega)$ is mainly associated with interband transitions of 3D Dirac electrons. A sudden drop in $A(\omega)$ at low energies implies the modification of the band structures within an energy range, namely the bandgap. *D, Inset* depicts the interband absorption in gapped $ZrTe_5$.

the linearly dispersing conduction and valence band degenerate at the Γ point were suggested to exist in this material by previous angle-resolved photon emission spectroscopy, transport, and optical experiments (38–41). Considering that (*i*) our $ZrTe_5$ thick crystals were experimentally shown to be Dirac semimetals hosting 3D massless Dirac fermions, (*ii*) $ZrTe_5$ monolayers were theoretically predicted to be quantum spin Hall insulators, and (*iii*) the bulk state of $ZrTe_5$ is very sensitive to its interlayer distance, which might be a discrepancy in different samples (33, 40); it is significant to quantitatively verify whether 3D massive Dirac fermions with a bandgap and nearly linear bulk-band dispersions can be realized in dramatically thinned flakes of our $ZrTe_5$ crystals.

Infrared spectroscopy is a bulk-sensitive experimental technique for studying low-energy excitations of a material. Here, to investigate the bulk-band inversion and the nature of the bulk fermions in $ZrTe_5$, we measured the infrared transmission spectra $T(\omega, B)$ of its multilayer flake with thickness d ~180 nm at magnetic fields applied along the wave vector of the incident light (*Materials and Methods* and *Supporting Information*). A series of intra- and inter-LL transitions are present in the relative transmission spectra $T(B)/T(B_0 = 0\text{ T})$ of the $ZrTe_5$ flake. The linear $\sqrt{B}$ dependence of the LL transition energies at $B \leq 4$ T and the nonzero intercept of the LL transitions at $B = 0$ T, combined with the linear relationship between the zero-magnetic-field optical absorption and the photon energy, indicates 3D massive Dirac fermions with nearly linear band dispersions in the $ZrTe_5$ flake. Moreover, a 3D massive Dirac model with a bandgap of ~10 meV can quantitatively explain the magnetic-field dependence of the measured LL transition energies very well. At high magnetic fields, we observed fourfold splittings of the LL transitions. In addition, our analysis of the split LL transitions shows that the intra-LL transitions, which are associated to the two zeroth LLs and disappear at $B \sim 2.5$ T, reemerge at $B > 17$ T. Considering that the zeroth LL crossing in a Zeeman field would make the two zeroth bulk LLs intersect with the chemical potential here and then alter the carrier occupation on the zeroth LLs, we attribute the reemergence of the intra-LL transitions in the $ZrTe_5$ flake to the energy crossing of its two zeroth bulk LLs, which originates from the bulk-band inversion. These results strongly support the theoretically predicted 3D TI states in 3D $ZrTe_5$ crystals.

Results

Three-Dimensional Massive Dirac Fermions. At zero magnetic field, the measured absolute transmission $T(\omega)$ corresponds to the absorption coefficient: $A(\omega) = -[\ln T(\omega)]/d$, where d is the thickness of the sample and ω is the photon energy (see the methods section of ref. 42). In solids, the absorption coefficient is determined by the joint density of state $D(\omega)$: $A(\omega) \propto D(\omega)/\omega$. Three-dimensional electron systems with linear band dispersions along three momentum directions have the $D(\omega)$ proportional to ω^2, and for 2D linear dispersions, $D(\omega) \propto \omega$. Thus, in stark contrast to the ω-independent absorption of 2D Dirac materials like graphene (43), the linear ω dependence of $A(\omega)$ in Fig. 1*D* indicates 3D linear band dispersions in $ZrTe_5$. Moreover, at low energies, the absorption coefficient apparently deviates from the linear relationship with ω, implying the opening of a bandgap at the original Dirac point. The 3D linear band dispersions, together with the possible bandgap, suggest the presence of 3D massive Dirac fermions in the exfoliated $ZrTe_5$ flake.

To confirm the 3D massive Dirac fermions in $ZrTe_5$, we further performed infrared transmission experiments at magnetic fields applied perpendicular to the *ac* plane (*xy* plane) of the crystal (Faraday geometry). The low-field relative transmission $T(B)/T(B_0 = 0\text{ T})$ spectra in Fig. 2*A* show seven dip features T_n ($1 \leq n \leq 7$) directly corresponding to the absorption peaks of LL

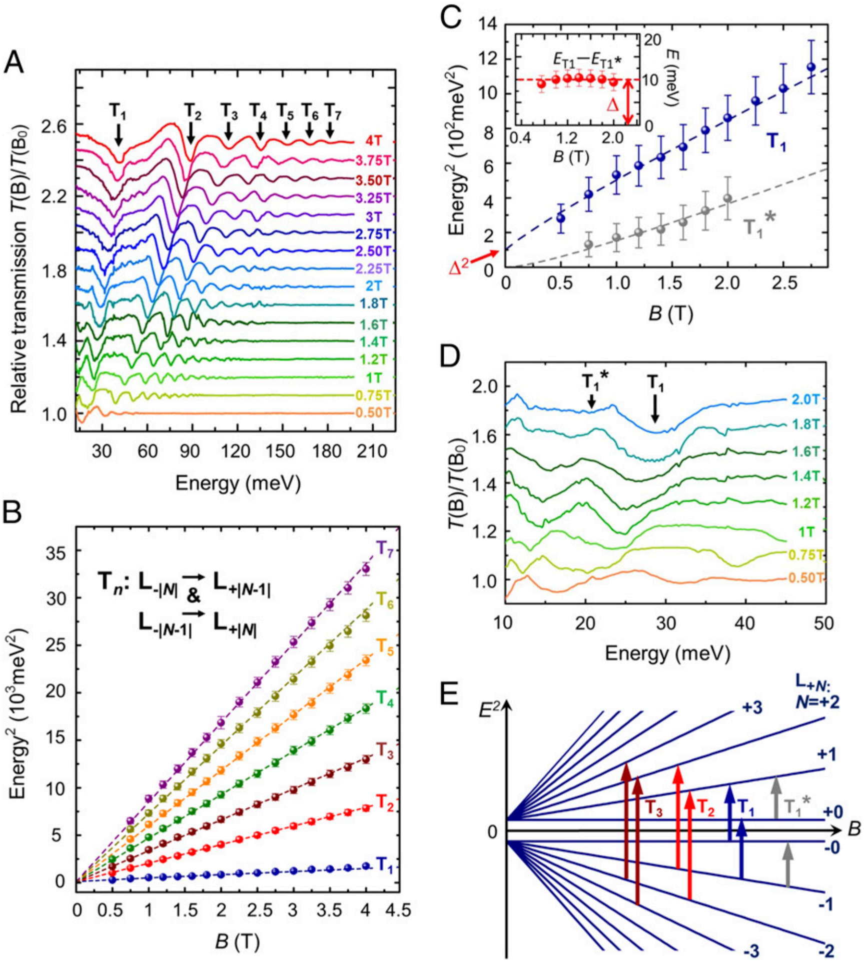

Fig. 2. Low-magnetic-field Landau level transitions in $ZrTe_5$. (*A*) Absorption features T_n ($1 \le n \le 7$) in *T(B)/T(B*$_0$*)* spectra. The spectra are displaced from one another by 0.1 for clarity. (*B, C*) Squares of T_n and T_1* energies plotted as a function of magnetic field ($B \le 4$ T). T_n correspond to the interband LL transitions: $LL_{-|N|} \to LL_{+|N-1|}$ (or $LL_{-|N-1|} \to LL_{+|N|}$). The nonzero $E^2_{T_1}(B)$ at zero field reveals a bandgap Δ. *C, Inset* shows the energy difference between T_1 and T_1*, which equals to the bandgap. (*D*) Absorption features T_1* in *T(B)/T(B*$_0$*)* spectra. T_1*, which is located at energies lower than T_1, arises from the intraband LL transition $LL_{+0} \to LL_{+1}$ (or $LL_{-1} \to LL_{-0}$). (*E*) Schematic of the Landau level spectrum without a Zeeman splitting and the allowed optical transitions, shown in a E^2–B plot.

transitions. All of these dip features systematically shift to higher energies, as the magnetic field increases. Here, we define the energy positions of the transmission minima in $T(B)/T(B_0)$ as the absorption energies, which is a usual definition in thin film systems, such as Bi_2Se_3 films and graphene. Then, we plotted the square of the T_n energies ($E^2_{T_n}$) as a function of magnetic field in Fig. 2*B*. The linear B dependence of $E^2_{T_n}$ (i.e., linear $\sqrt{B}$ dependence of E_{T_n}) reveals the LL transitions of Dirac fermions (31, 44, 45). In Fig. 2*C*, the nonzero intercept of the linear fit to $E^2_{T_1}$ at zero magnetic field is an important signature of a nonzero Dirac mass or a bandgap (31). Therefore, the linear relationship between $E^2_{T_n}$ and B, together with the nonzero intercept, provides further evidence for 3D massive Dirac fermions in the $ZrTe_5$ flake.

To quantitatively check the 3D massive Dirac fermions in the $ZrTe_5$ flake, we use a 3D massive Dirac Hamiltonian, which was derived from the low-energy effective $k \cdot p$ Hamiltonian based on the spin–orbital coupling, the point group and time-reversal symmetries in $ZrTe_5$, and includes the spin degree of freedom (40). According to the 3D massive Dirac Hamiltonian expanded to the linear order of momenta, we can obtained the nearly linear band dispersions of $ZrTe_5$ at zero magnetic field: $E(k_{x,y,z}) = \pm\sqrt{\hbar^2(k_x^2 v_x^2 + k_y^2 v_y^2 + k_z^2 v_z^2) + (\Delta/2)^2}$, where $k_{x,y,z}$ are the wave vectors in momentum space, $v_{x,y,z}$ are the Fermi velocities along three momentum directions, Δ is the bandgap and describes the mass of Dirac fermions $m^D_{x,y,z} = \Delta/(2v^2_{x,y,z})$ and $\hbar$ is Planck's constant divided by 2π. In a magnetic field applied perpendicular to the *ac* plane, the LL spectrum of $ZrTe_5$ without considering Zeeman effects has the form:

$$E_N(k_z) = \pm\,\delta_{N,0}\sqrt{(\Delta/2)^2 + (v_z\hbar k_z)^2} + \mathrm{sgn}(N)\sqrt{2e\hbar v_F^2 B|N| + (\Delta/2)^2 + (v_z\hbar k_z)^2}, \qquad [1]$$

where v_F is the effective Fermi velocity of LLs, the integer N is Landau index, $\delta_{N,0}$ is the Kronecker delta function, sgn(N) is the sign function, and e is the elementary charge. The $\sqrt{B}$ dependence is a hallmark of Dirac fermions (31, 44, 45). According to Eq. **1**, the magnetic field makes the 3D linear band dispersions evolve into a series of 1D non-equally-spaced Landau levels (or bands), which disperse with the momentum component along the field direction. Specifically, because the 3D massive Dirac Hamiltonian of $ZrTe_5$ involves the spin degree of freedom of this system, two zeroth LLs indexed by $N = +0$ and $N = -0$ locate at the hole and electron band extrema, respectively, and have energy dispersions $E_{\pm 0}(k_z) = \pm\sqrt{(\Delta/2)^2 + (v_z\hbar k_z)^2}$, which is different from the case that when the spin degree of freedom was not considered in materials with the hexagonal lattice, only one zeroth nondegenerate Landau level is present in each valley (46). The optical selection rule for $ZrTe_5$ only allows the LL transitions from LL_N to $LL_{N'}$: $\Delta N = |N| - |N'| = \pm 1$ and with the k_z-momentum difference $\Delta k_z = 0$ (40). Due to the singularities of the density of states (DOS) at $k_z = 0$, magneto-optical response here, which is determined by the joint DOS, should be mainly contributed by the LL transitions at $k_z = 0$ (29, 40). Thus, the energies of the interband LL (inter-LL) transitions $LL_{-|N|} \rightarrow LL_{+|N-1|}$ (or $LL_{-|N-1|} \rightarrow LL_{+|N|}$) and the intraband LL (intra-LL) transitions $LL_{+|N-1|} \rightarrow LL_{+|N|}$ (or $LL_{-|N|} \rightarrow LL_{-|N-1|}$), E_N^{Inter} and E_N^{Intra} at $k_z = 0$, are given by:

$$E_N^{Inter} = \sqrt{2e\hbar v_F{}^2 B|N| + (\Delta/2)^2} + \sqrt{2e\hbar v_F{}^2 B|N-1| + (\Delta/2)^2} \quad [2]$$

$$E_N^{Intra} = \sqrt{2e\hbar v_F{}^2 B|N| + (\Delta/2)^2} - \sqrt{2e\hbar v_F{}^2 B|N-1| + (\Delta/2)^2}. \quad [3]$$

From T_1 to T_7, the slopes of the linear fits to $E^2_{T_n}$ in Fig. 2*B* scale as 1: 5.7: 9.3: 13.1: 16.7: 20.5: 24.1, respectively, which is close to the approximate ratio of the theoretical inter-LL transition energies based on Eq. **2**, 1: $(\sqrt{2}+\sqrt{1})^2$ (~ 5.8): $(\sqrt{3}+\sqrt{2})^2$ (~ 9.9): $(\sqrt{4}+\sqrt{3})^2$ (~ 13.9): $(\sqrt{5}+\sqrt{4})^2$ (~ 17.9): $(\sqrt{6}+\sqrt{5})^2$ (~ 21.9): $(\sqrt{7}+\sqrt{6})^2$ (~ 25.9). Therefore, the absorption features T_n are assigned as the inter-LL transitions: $LL_{-|N-1|} \rightarrow LL_{+|N|}$ (or $LL_{-|N|} \rightarrow LL_{+|N-1|}$) (Fig. 2*B*) and we have $n = |N|$, where $1 \le n \le 7$. Fitting $E^2_{T_n}$ based on Eq. **2** from a least square fit yields a bandgap $\Delta \sim 10 \pm 2$ meV, the effective Fermi velocities $v_F^{T_1} \approx (4.76 \pm 0.04) \times 10^5$ m/s and $v_F^{T_{2\le n\le 7}} \approx (5.04–4.95 \pm 0.04) \times 10^5$ m/s (*Supporting Information*).

As another signature of the bandgap or the nonzero Dirac mass, the absorption feature $T_1{}^*$ is present at energies lower than the lowest-energy inter-LL transition T_1 in Fig. 2*D*. The feature $T_1{}^*$ is attributed to the intra-LL transition $LL_{+0} \rightarrow LL_{+1}$ (or $LL_{-1} \rightarrow LL_{-0}$), illustrated by the gray arrows in Fig. 2*E* (*Supporting Information*). According to Eqs. **2** and **3**, the energy difference $(E_{T1} - E_{T1^*})$ between the transitions T_1 and $T_1{}^*$ in the inset of Fig. 2*C* directly gives the bandgap value $\Delta = E_{T1} - E_{T1}{}^* \approx 10 \pm 2$ meV, which is consistent with the value obtained by the above fitting. Furthermore, the field dependence of the $T_1{}^*$ energy in Fig. 2*C* can be well fitted by Eq. **3** with $\Delta \sim 10 \pm 2$ meV and $v_F^{T_1{}^*} \approx (4.63 \pm 0.04) \times 10^5$ m/s.

The carrier-charge mobility μ in the $ZrTe_5$ flake can be calculated using the general equation (47): $\mu = e\hbar/(\Gamma m^*)$, where Γ is the transport scattering rate and m^* is the carrier effective mass on the anisotropic Fermi surface (48, 49). Here, the transport scattering rate Γ within the *ac* plane can be roughly estimated from the width of the T_1 feature at low fields: $\Gamma \sim 9$ meV at $B = 0.5$ T. Moreover, considering the absence of Pauli blocking of the T_1 transition at $B = 0.5$ T, we get the Fermi energy in $ZrTe_5$, $E_F < |E_{LL+1(\text{or } -1)}| = E_{T1} \approx 15$ meV (*Supporting Information*), which means the Fermi level in our sample is quite close to the band extrema. In this case, the average effective mass m^* of the carriers within the *ac* plane can be described by (30): $m_{ac}{}^* \approx \Delta/[2(v_F^{ac})^2] \approx 3.54 \times 10^{-33}$ kg $\approx 0.00389\, m_0$, where m_0 is the free electron mass and the average Fermi velocity within the *ac* plane v_F^{ac} is approximately equal to the effective Fermi velocity of the LLs, $v_F^{ac} \approx 4.76 \times 10^5$ m/s. Finally, we can estimate the mobility of the carriers within the *ac* plane of our $ZrTe_5$ sample: $\mu \approx 33{,}000$ cm^2/(V · s), which is comparable to those in graphene/h-BN heterostructures (50, 51).

Buk-Band Inversion. As shown in Fig. 3*A*, applying a higher magnetic field enables us to observe the splitting of the T_1 transition, which indicates a nonnegligible Zeeman effect in $ZrTe_5$ (40). For TIs, due to the Zeeman field, each LL except the two zeroth LLs splits into two sublevels with opposite spin states, while the LL_{-0} and LL_{+0} are spin-polarized and have spin-up and -down state, respectively (3, 29). The energy of the sublevel has the form (40):

$$E_{N,\xi} = E_N(k_z = 0) + 1/2\xi g_N B, \quad [4]$$

where ξ is equal to +1 for spin-up and –1 for spin-down and g_N is the effective Landé *g* factor of LL_N. The spin-orbit coupling (SOC) in $ZrTe_5$ mixes the spin states of the two sublevels, so two extra optical transitions between the sublevels with different spin indices become possible. The inter- and intra-LL transition energies including the Zeeman effect can be written as (40):

$$E^{Inter}_{N,\xi,\xi'} = E_N^{Inter} + 1/2\left(\xi g_N - \xi' g_{-(N-1)}\right)B \quad [5]$$

$$E^{Intra}_{N,\xi,\xi'} = E_N^{Intra} + 1/2\left(\xi g_N - \xi' g_{(N-1)}\right)B, \quad [6]$$

where ξ and ξ' correspond to the spin states of the two sublevels, respectively.

Fig. 3*B* displays the false-color map of the $-\ln[T(B)/T(B_0)]$ spectra of the $ZrTe_5$ flake. Interestingly, a cusplike feature around 18 T, which is indicated by a white arrow, can be observed in Fig. 3*C* (i.e., the magnified image of a region in Fig. 3*B*). To quantitatively investigate the physical meaning of this cusplike feature, we plot the energies of the four split T_1 transitions [i.e., 1α, 1β, 1γ, and 1δ (green dots)] around 16 T in Fig. 3*B*, which are defined by the onsets of the absorption features due to the Zeeman splitting (see figure 3 of the Supplemental Material of ref. 40 and *Supporting Information*). As displayed by the green dashed lines in Fig. 3*B*, fitting the energy traces of the inter-LL transitions, 1α, 1β, 1γ, and 1δ, based on Eq. **5** with the obtained values of the Fermi velocity $v_F^{T_1}$ and the bandgap Δ yields the *g* factors of the two zeroth LLs and $LL_{\pm 1}$: $g_{eff}(LL_{+0}) = g_{eff}(LL_{-0}) \sim 11.1$, $g_{eff}(LL_{-1}) \sim 31.1$ and $g_{eff}(LL_{+1}) \sim 9.7$ [or $g_{eff}(LL_{+1}) \sim 31.1$ and $g_{eff}(LL_{-1}) \sim 9.7$] (*Supporting Information*).

It is known that as a hallmark of TIs, the band inversion causes the exchange of the characteristics between the valence- and conduction-band extrema (2, 6, 28), so as shown in Fig. 1*A* and 3*D*, the LL_{-0} and LL_{+0}, which come from the inverted band extrema, have reversed spin states and cross at a critical magnetic field (3, 29). According to Eq. **4** with the above values of $g_{eff}(LL_{\pm 0})$ and Δ, we estimated the critical magnetic field $B_c \sim 17$ T. In Fig. 2 *A* and *D*, the disappearance of the intra-LL transition $T_1{}^*$ around $B \sim 2.5$ T indicates that LL_{+0} (or LL_{-0}) becomes fully depleted (or occupied) with increasing magnetic field and that at $B > 2.5$ T, the chemical potential of $ZrTe_5$ can be considered to be located at zero energy. In this case, the two zeroth LLs intersect with the chemical potential at the same magnetic field B_c. More importantly, this intersection means at $B > B_c \sim 17$ T, LL_{-0} and LL_{+0} becomes empty and occupied, respectively, which leads to the gradual replacement of the inter-LL transitions T_1, 1α, 1β, 1γ, and 1δ, by the intra-LL transitions $T_1{}^*$, 1χ, 1λ, 1θ, and 1ε, explained in Fig. 3*D*. Furthermore, in Fig. 3*B*, the energy traces of the four split transitions (gray dots) observed at $B > 17$ T are shown to follow the white theoretical curves for the intra-LL transitions $T_1{}^*$, which are based on Eq. **6**. Therefore, the four split transitions observed at $B > 17$ T in Fig. 3*B* can be assigned as the intra-LL transitions $T_1{}^*$, 1χ, 1λ, 1θ, and 1ε. Because the energy traces of the split intra-LL transitions $T_1{}^*$ deviate markedly from those of the inter-LL transitions T_1, the reemergence of the $T_1{}^*$ transitions at $B > 17$ T causes the cusplike feature, which provides experimental evidence for the bulk-band inversion in the $ZrTe_5$ flake.

In summary, using magnetoinfrared spectroscopy, we have investigated the Landau level spectrum of the multilayer $ZrTe_5$ flake. The magnetic-field dependence of the LL transition energies

APPLIED PHYSICAL SCIENCES

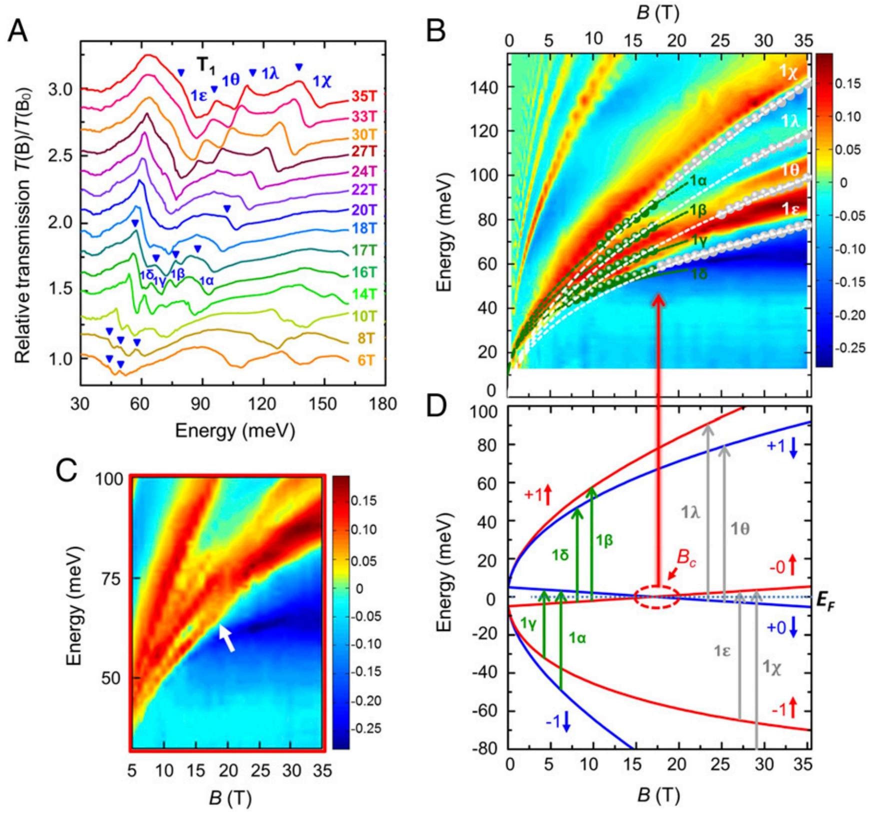

Fig. 3. Crossing of the two zeroth LLs of $ZrTe_5$. (*A*) Split T_1 transitions in the $T(B)/T(B_0)$ spectra at $B \geq 6$ T. The energies of the split T_1 transitions are defined by the onsets of the dip features indicated by the blue triangles. Around 16 T, four modes are present. Four modes reemerge around 27 T. (*B*) Color scale map of the $-\ln[T(B)/T(B_0)]$ spectra as a function of magnetic field and energy. (*C*) Magnified view of a region in *B* to better present the cusplike feature that is indicated by a white arrow around 18 T. The measured T_1 (green dots) and T_1* (gray dots) energies are plotted as a function of magnetic field in *B*. Here, the green and gray dots in *B* can be extracted from the lower-energy edges (i.e., the onsets) of the peak-feature traces in the color intensity plots (i.e., *B* and *C*) of the $-\ln[T(B)/T(B_0)]$ spectra. These dots in *B* have the intensities of the color scale, respectively: 0.025 for 1α, 1β, 1γ, and 1θ, –0.025 for 1δ, 1χ, and 1λ and –0.075 for 1ε. The theoretical T_1 and T_1* energies, based on Eqs. **5** and **6** with the *g* factors: $g_{eff}(LL_{-1}) = 31.1$, $g_{eff}(LL_{+1}) = 9.7$, and $g_{eff}(LL_{+0}) = g_{eff}(LL_{-0}) = 11.1$, the bandgap $\Delta = 10$ meV, the Fermi velocities $v_F^{T_1} = 4.76 \times 10^5$ m/s, and $v_F^{T_1*} = 4.63 \times 10^5$ m/s, are shown by the green and gray dashed curves, respectively. (*D*) Schematic of the split T_1 (green arrows) and T_1* (gray arrows) transitions. The LL spectrum is produced with the above values of the *g* factors, the bandgap and the Fermi velocity $v_F^{T_1}$. The two zeroth LLs cross at a critical magnetic field $B_c \sim 17$ T. The chemical potential is roughly at zero energy when the magnetic field is high enough. At $B > B_c$, the interband LL transitions (1α, 1β, 1γ, and 1δ) are gradually replaced by the intraband LL transitions (1χ, 1θ, 1λ, and 1ε), which causes the cusplike feature shown in *C*.

here, together with the photon-energy dependence of the absorption coefficient at zero field, quantitatively demonstrates 3D massive Dirac fermions with nearly linear dispersions in the $ZrTe_5$ flake. Due to the Zeeman splitting of the LLs, the energy splitting of the LL transitions was observed at $B \geq 6$ T. Interestingly, the intra-LL transitions T_1* reemerge at $B > 17$ T. We propose that the reemergence of the T_1* transitions results from the band-inversion-induced crossing of the two zeroth LLs, LL_{+0} and LL_{-0}. Our results make $ZrTe_5$ flakes good contenders for 3D TIs. Moreover, due to the 3D massive Dirac-like dispersions and the high bulk-carrier mobility [$\sim 33{,}000\ cm^2/(V \cdot s)$], the $ZrTe_5$ flake can also be viewed as a 3D analog of gapped graphene, which enables us to deeply investigate exotic quantum phenomena.

Materials and Methods

Sample Preparation and Characterizations. Bulk single crystals of $ZrTe_5$ were grown by Te flux method. The elemental Zr and Te with high purity were sealed in an evacuated double-walled quartz ampule. The raw materials were heated at 900 °C and kept for 72 h. Then they were cooled slowly down to 445 °C and heated rapidly up to 505 °C. The thermal–cooling cycling between 445 and 505 °C lasts for 21 d to remelt the small size crystals. The multilayer $ZrTe_5$ flake (*ac* plane) for magnetotransmission measurements were fabricated by mechanical exfoliation, and deposited onto double-side-polished SiO_2/Si substrates with 300 nm SiO_2. The flake thickness ~180 nm and the chemical composition were characterized by atomic force microscopy (AFM) and energy dispersion spectroscopy (EDS), respectively (*Supporting Information*).

Infrared Transmission Measurements. The transmission spectra were measured at about 4.5 K in a resistive magnet in the Faraday geometry with magnetic field applied in parallel to the wave vector of incident light and the crystal *b* axis. Nonpolarized IR light (provided and analyzed by a Fourier transform spectrometer) was delivered to the sample using a copper light pipe. A composite Si bolometer was placed directly below the sample to detect the transmitted light. The diameter of IR focus on the sample is ~ 0.5–1 mm. Owing to the mismatch between the size of the IR focus and the $ZrTe_5$ flake, an aluminum aperture was placed around the sample. The transmission spectra are shown at energies above 10 meV, corresponding to wavelengths shorter than 124 μm. The wavelength of infrared light here is smaller than the size of the measured sample, and thus the optical constants can be used for a macroscopic description of the data.

ACKNOWLEDGMENTS. We thank X. C. Xie, F. Wang, Z. Fang, M. Orlita, M. Potemski, H. M. Weng, L. Wang, C. Fang, and X. Dai for very helpful discussions. We acknowledge support from the Hundred Talents Program of Chinese Academy of Sciences, the National Key Research and Development Program of China (Project 2016YFA0300600), the European Research Council (ERC ARG MOMB Grant 320590), the National Science Foundation of China (Grants 11120101003 and 11327806), and the 973 project of the Ministry of Science and Technology of China (Grant 2012CB821403). A portion of this work was performed in National High Magnetic Field Laboratory, which is supported by National Science Foundation

Cooperative Agreement DMR-1157490 and the State of Florida. Work at Brookhaven was supported by the Office of Basic Energy Sciences, Division of Materials Sciences and Engineering, US Department of Energy, through Contract DE-SC00112704.

1. Kane CL, Mele EJ (2005) Z_2 topological order and the quantum spin Hall effect. *Phys Rev Lett* 95(14):146802.
2. Bernevig BA, Hughes TL, Zhang SC (2006) Quantum spin Hall effect and topological phase transition in HgTe quantum wells. *Science* 314(5806):1757–1761.
3. König M, et al. (2007) Quantum spin hall insulator state in HgTe quantum wells. *Science* 318(5851):766–770.
4. Fu L, Kane CL, Mele EJ (2007) Topological insulators in three dimensions. *Phys Rev Lett* 98(10):106803.
5. Moore JE, Balents L (2007) Topological invariants of time-reversal-invariant band structures. *Phys Rev B* 75:121306.
6. Zhang H, et al. (2009) Topological insulators in Bi_2Se_3, Bi_2Te_3 and Sb_2Te_3 with a single Dirac cone on the surface. *Nat Phys* 5:438–442.
7. Hsieh D, et al. (2008) A topological Dirac insulator in a quantum spin Hall phase. *Nature* 452(7190):970–974.
8. Chen YL, et al. (2009) Experimental realization of a three-dimensional topological insulator, Bi_2Te_3. *Science* 325(5937):178–181.
9. Wan XG, Turner AM, Vishwanath A, Savrasov SY (2011) Topological semimetal and Fermi-arc surface states in the electronic structure of pyrochlore iridates. *Phys Rev B* 83:205101.
10. Young SM, et al. (2012) Dirac semimetal in three dimensions. *Phys Rev Lett* 108(14): 140405.
11. Wang ZJ, et al. (2012) Dirac semimetal and topological phase transitions in A_3Bi (A = Na, K, Rb). *Phys Rev B* 85:195320.
12. Wang ZJ, et al. (2013) Three-dimensional Dirac semimetal and quantum transport in Cd_3As_2. *Phys Rev B* 88:125427.
13. Liu ZK, et al. (2014) Discovery of a three-dimensional topological Dirac semimetal, Na_3Bi. *Science* 343(6173):864–867.
14. Neupane M, et al. (2014) Observation of a three-dimensional topological Dirac semimetal phase in high-mobility Cd_3As_2. *Nat Commun* 5:3786.
15. Jeon S, et al. (2014) Landau quantization and quasiparticle interference in the three-dimensional Dirac semimetal Cd_3As_2. *Nat Mater* 13(9):851–856.
16. Liang T, et al. (2015) Ultrahigh mobility and giant magnetoresistance in the Dirac semimetal Cd_3As_2. *Nat Mater* 14(3):280–284.
17. He LP, et al. (2014) Quantum transport evidence for the three-dimensional Dirac semimetal phase in Cd_3As_2. *Phys Rev Lett* 113(24):246402.
18. Borisenko S, et al. (2014) Experimental realization of a three-dimensional Dirac semimetal. *Phys Rev Lett* 113(2):027603.
19. Liu ZK, et al. (2014) A stable three-dimensional topological Dirac semimetal Cd_3As_2. *Nat Mater* 13(7):677–681.
20. Burkov AA, Balents L (2011) Weyl semimetal in a topological insulator multilayer. *Phys Rev Lett* 107(12):127205.
21. Weng H, et al. (2015) Weyl semimetal phase in non-centrosymmetric transition metal monophosphides. *Phys Rev X* 5:011029.
22. Huang SM, et al. (2015) A Weyl Fermion semimetal with surface Fermi arcs in the transition metal monopnictide TaAs class. *Nat Commun* 6:7373.
23. Xu SY, et al. (2015) Discovery of a Weyl fermion semimetal and topological Fermi arcs. *Science* 349(6248):613–617.
24. Lv BQ, et al. (2015) Observation of Weyl nodes in TaAs. *Nat Phys* 11:724–727.
25. Yang LX, et al. (2015) Weyl semimetal phase in the non-centrosymmetric compound TaAs. *Nat Phys* 11:728–732.
26. Xu SY, et al. (2015) Discovery of a Weyl fermion state with Fermi arcs in niobium arsenide. *Nat Phys* 11:748–754.
27. Shekhar C, et al. (2015) Extremely large magnetoresistance and ultrahigh mobility in the topological Weyl semimetal candidate NbP. *Nat Phys* 11:645–649.
28. Liu CX, et al. (2010) Model Hamiltonian for topological insulators. *Phys Rev B* 82: 045122.
29. Orlita M, et al. (2015) Magneto-optics of massive Dirac fermions in bulk Bi_2Se_3. *Phys Rev Lett* 114(18):186401.
30. Hunt B, et al. (2013) Massive Dirac fermions and Hofstadter butterfly in a van der Waals heterostructure. *Science* 340(6139):1427–1430.
31. Chen Z-G, et al. (2014) Observation of an intrinsic bandgap and Landau level renormalization in graphene/boron-nitride heterostructures. *Nat Commun* 5:4461.
32. Fjellvåg H, Kjekshus A (1986) Structural properties of $ZrTe_5$ and $HfTe_5$ as seen by powder Diffraction. *Solid State Commun* 60:91–93.
33. Weng H, et al. (2014) Transition-metal pentatelluride $ZrTe_5$ and $HfTe_5$: A paradigm for large-gap quantum spin Hall insulators. *Phys Rev X* 4:011002.
34. Niu J, et al. (2015) Electrical transport in nano-thick $ZrTe_5$ sheets: From three to two dimensions. arXiv:1511.09315.
35. Li X-B, et al. (2016) Experimental observation of topological edge states at the surface step edge of the topological insulator $ZrTe_5$. *Phys Rev Lett* 116(17):176803.
36. Wu R, et al. (2016) Experimental evidence of large-gap two-dimensional topological insulator on the surface of $ZrTe_5$. *Phys Rev X* 6:021017.
37. Zhang Y, et al. (2016) Electronic evidence of temperature-induced Lifshitz transition and topological nature in $ZrTe_5$. arXiv:1602.03576.
38. Li Q, et al. (2016) Chiral magnetic effect in $ZrTe_5$. *Nat Phys* 12:550–554.
39. Chen RY, et al. (2015) Optical spectroscopy study of the three-dimensional Dirac semimetal $ZrTe_5$. *Phys Rev B* 92:075107.
40. Chen RY, et al. (2015) Magnetoinfrared spectroscopy of Landau levels and Zeeman splitting of three-dimensional massless Dirac fermions in $ZrTe_5$. *Phys Rev Lett* 115(17): 176404.
41. Zheng G, et al. (2016) Transport evidence for the three-dimensional Dirac semimetal phase in $ZrTe_5$. *Phys Rev B* 93:115414.
42. Orlita M, et al. (2014) Observation of three-dimensional massless Kane fermions in a zinc-blende crystal. *Nat Phys* 10:233–238.
43. Li ZQ, et al. (2008) Dirac charge dynamics in graphene by infrared spectroscopy. *Nat Phys* 4:532–535.
44. Sadowski ML, Martinez G, Potemski M, Berger C, de Heer WA (2006) Landau level spectroscopy of ultrathin graphite layers. *Phys Rev Lett* 97(26):266405.
45. Jiang Z, et al. (2007) Infrared spectroscopy of Landau levels of graphene. *Phys Rev Lett* 98(19):197403.
46. Liang T, et al. (2013) Evidence for massive bulk Dirac fermions in $Pb_{1-x}Sn_xSe$ from Nernst and thermopower experiments. *Nat Commun* 4:2696.
47. Issi J-P, et al. (2014) Electron and phonon transport in graphene in and out of the bulk. *Physics of Graphene*, eds Aoki H, Dresselhaus MS (Springer, Switzerland), pp 65–112.
48. Kamm GN, Gillespie DJ, Ehrlich AC, Wieting TJ, Levy F (1985) Fermi surface, effective masses, and Dingle temperatures of $ZrTe_5$ as derived from the Shubnikov-de Haas effect. *Phys Rev B Condens Matter* 31(12):7617–7623.
49. Yuan X, et al. (2016) Observation of quasi-two-dimensional Dirac fermions in $ZrTe_5$. *NPG Asia Materials* 8:e325.
50. Ponomarenko LA, et al. (2013) Cloning of Dirac fermions in graphene superlattices. *Nature* 497(7451):594–597.
51. Dean CR, et al. (2013) Hofstadter's butterfly and the fractal quantum Hall effect in moiré superlattices. *Nature* 497(7451):598–602.

Supporting Information

Chen et al. 10.1073/pnas.1613110114

Basic Characteristics of the $ZrTe_5$ Sample

We show the thickness of the $ZrTe_5$ flake characterized by atomic force microscopy and the energy dispersion X-ray spectra of the $ZrTe_5$ flake in Fig. S1. The multilayer flake studied in the main text has the thickness $d \sim 180$ nm. For our sample, the atom ratio, Zr: Te ~ 1: 5.

Bandgap and Effective Fermi Velocity Obtained by Least Squares Fit

Using the method of least squares fit, we fit the measured Landau level transition energies of the $ZrTe_5$ flake present in Fig. 2 *B* and *C*, based on Eqs. **2** and **3** in the main text. The two parameters, bandgap Δ and the effective Fermi velocity v_F, are assumed to be field independent. As shown in Fig. S2*A*, the fit to the T_1 transition data with Δ and v_F as free parameters deduces a gap $\Delta \sim 10 \pm 2$ meV and an effective Fermi velocity $v_F^{T_3} \approx (4.76 \pm 0.01) \times 10^5$ m/s. For the other transitions, T_2, T_3, T_4, T_5, T_6, and T_7, we fit the data using two approaches (*i*): setting both Δ and v_F as free parameters, and (*ii*) fixing the gap value $\Delta = 10$ meV and allowing v_F to be a free parameter. As shown in Fig. S2 *C–H*, for T_2, T_3, T_4, T_5, T_6, and T_7, these two approaches produce the similar fits within the error bars of the data and the similar values of the sum of square residuals χ^2, which are the value differences between the measured data and the fitting curve. Therefore, the fitting results, which were deduced from the above two methods, indicate that the T_2, T_3, T_4, T_5, T_6, and T_7 transition energies at low fields ($B \le 4$ T) have a consistent gap $\Delta \sim 10 \pm 2$ meV, which is similar to the gap value deduced from the T_1 transition. From the gap value $\Delta \sim 10 \pm 2$ meV, we can obtain comparable Fermi velocities of the T_2, T_3, T_4, T_5, T_6, and T_7 transitions, ranging from $(4.95 \pm 0.04) \times 10^5$ m/s to $(5.04 \pm 0.04) \times 10^5$ m/s, as shown in Table S1.

When Δ and v_F are field independent, the least squares fit for the T_1 transition based on Eq. **2** in the main text yields $\chi_2^2 > \chi_1^2$, where χ_1^2 and χ_2^2 correspond to the sum of squared residuals in the approaches (*i*) and (*ii*), respectively. As displayed in Fig. S2*A*, the first approach can describe the T_1 transition [with $\Delta' = 7 \pm 1$ meV and $v_F^{T1'} \approx (5.18 \pm 0.01) \times 10^5$ m/s] better than the second approach with $\Delta = 10$ meV. Given that all of the bandgap extracted from the LL transitions correspond to the zero-field gap of the $ZrTe_5$ flake, we assume the same gap value of 10 ± 2 meV for the T_1 transition and attribute the deviations of the T_1 transition from the behaviors described by Eq. **2** to an effective Fermi velocity v_F^{T1}. Therefore, from the second least squares fit approach, we obtained the effective Fermi velocity for the T_1 transition, $v_F^{T1} \approx (4.76 \pm 0.01) \times 10^5$ m/s, which is smaller than the fitted values of v_F^{Tn} $(7 \ge n \ge 2)$.

For T_1*, the first approach for fitting deduces the bandgap $\Delta' = 4 \pm 1$ meV and the Fermi velocity $v_F^{T1*'} \approx (4.07 \pm 0.09) \times 10^5$ m/s, and the second approach with fixed $\Delta = 10$ meV has the Fermi velocity $v_F^{T1*} \approx (4.63 \pm 0.09) \times 10^5$ m/s. A smaller gap value was obtained from the first method, which is consistent with the case in T_1, but these two approaches have similar values of the sum of square residuals χ^2: $\chi_1^2 \approx \chi_2^2$. Because the bandgap extracted from T_1* corresponds to the zero-field gap and should be the same as those from the other LL transitions, we also attribute the deviations of the T_1* transition from the behaviors described by Eq. **3** to an effective Fermi velocity. Thus, we obtained the effective Fermi velocity for the T_1* transition $v_F^{T1*} \approx (4.63 \pm 0.09) \times 10^5$ m/s.

Assigning T_1* to the Intra-LL transition from LL_{+0} (or LL_{-1}) to LL_{+1} (or LL_{-0})

To identify the nature of the T_1* feature, we plot the energy ratios between T_1 and T_1* for the $ZrTe_5$ flake in Fig. S3*A*. If there is no bandgap here, the T_1* feature, which locates at lower energies than the T_1 feature, should correspond to the intra-LL transition T* from LL_{+1} (or LL_{-2}) to LL_{+2} (or LL_{-1}), as illustrated in Fig. S3*B*. In this case, according to Eqs. **2** and **3** in the main text without a bandgap (namely, massless Dirac fermions), the energy ratio between the inter-LL transitions from LL_0 to LL_{+1} (or from LL_{-1} to LL_0) and the intra-LL transition T* should be ~2.415, as displayed by the magenta dashed line in Fig. S3*A*. However, the energy ratios between the measured T_1 and T_1* features, which are represented by the red stars, are much lower than 2.415. Instead, the red stars in Fig. S3*A* can be fitted by the red solid line corresponding to the energy ratio between the inter-LL transition from LL_{-0} to LL_{+1} (or from LL_{-1} to LL_{+0}) and the intra-LL transition from LL_{+0} to LL_{+1} (or from LL_{-1} to LL_{-0}), both of which are illustrated in Fig. 2*E* of the main text. Thus, the consistence between the red stars and the red solid line produced with a bandgap of 10 meV indicates that the observed T_1* feature originates from the intra-LL transition from LL_{+0} to LL_{+1} (or from LL_{-1} to LL_{-0}).

For the T_2 and T_1 features, if there is no bandgap, their theoretical energy ratio should correspond to the navy dashed line in Fig. S3*A*, which is produced by Eq. **2** of the main text. Definitely, this theoretical dashed line is much higher than the energy ratio between the measured T_2 and T_1 features, as represented by the blue stars. Instead, the blue stars can be fitted by the blue solid line based on Eq. **2** of the main text with a bandgap of 10 meV. So, the above two energy ratios between the observed LL transitions again reveal the existence of a bandgap in the $ZrTe_5$ flake.

Because the bandgap is comparable to the energies of T_1* and T_1 at magnetic fields $B \le 4.5$ T, the above two energy ratios between the observed LL transitions have distinctly smaller values than those obtained from the Eqs. **2** and **3** of the main text without a bandgap (namely, for massless Dirac fermions). However, if the bandgap is much smaller than the energies of the LL transitions, such as T_2 and T_3, it will be difficult to distinguish the difference in the energy ratios between the high-energy LL transitions for massive and massless Dirac fermions at high magnetic fields, which has been revealed by the purple stars, and the purple dashed and the solid lines for the energy ratio between T_3 and T_2.

Estimation of the Fermi Energy E_F from the Landau Level Transition

The Fermi energy in the $ZrTe_5$ flake can be estimated from the magnetotransmission data. According to Pauli's exclusion principle, the LL transitions T_1 and T_1*, LL_{-0} (or LL_{-1}) → LL_{+1} (or LL_{+0}) and LL_{-0} (or LL_{+0}) → LL_{-1} (or LL_{+1}), should be blocked if the LL_{+1} (or LL_{-1}) is fully occupied (or depleted), as the magnetic field decreases below a critical value B_{T1} (shown in Fig. S4*A*). Fig. 2 of the main text shows T_1 and T_1* can still be observed at 0.5 T, indicating $B_{T1} < 0.5$ T. Thus, as displayed in Fig. S4*B*, the Fermi level is between LL_{+0} and LL_{+1} (or between LL_{-1} and LL_{+0}) at $B = 0.5$ T and correspondingly, the Fermi energy E_F is not higher than 15 meV.

Calculation of the *g* Factors of the Landau Levels

According to Eq. **5** of the main text (with $\Delta = 10$ meV and $v_F^{T_1} = 4.76 \times 10^5$ m/s), we fit the energy traces of the split-T_1 transitions (i.e., 1α, 1β, 1γ, and 1δ) and then obtain the following four equations about the g factors of $LL_{\pm 0}$ and $LL_{\pm 1}$:

$$\text{For } 1\alpha \text{ transition: } \frac{1}{2}\left\{\left[g_{\text{eff}}(LL_{-1}) - g_{\text{eff}}(LL_{-0})\right]\right\} = 10.0 \quad \textbf{[S1]}$$

$$\text{For } 1\beta \text{ transition: } \frac{1}{2}\left\{\left[g_{\text{eff}}(LL_{+1}) - g_{\text{eff}}(LL_{+0})\right]\right\} = -0.7 \quad \textbf{[S2]}$$

$$\text{For } 1\gamma \text{ transition: } \frac{1}{2}\left\{\left[-g_{\text{eff}}(LL_{+1}) - g_{\text{eff}}(LL_{+0})\right]\right\} = -10.4 \quad \textbf{[S3]}$$

$$\text{For } 1\delta \text{ transition: } \frac{1}{2}\left\{\left[-g_{\text{eff}}(LL_{-1}) - g_{\text{eff}}(LL_{-0})\right]\right\} = -21.1 \quad \textbf{[S4]}$$

Solving Eqs. **S1–S4**, we obtain $g_{\text{eff}}(LL_{+0}) = g_{\text{eff}}(LL_{-0}) \sim 11.1$, $g_{\text{eff}}(LL_{-1}) \sim 31.1$ and $g_{\text{eff}}(LL_{+1}) \sim 9.7$. In another case with electron and hole LLs reversed, we have $g_{\text{eff}}(LL_{-1}) \sim 9.7$ and $g_{\text{eff}}(LL_{+1}) \sim 31.1$.

Definitions of the Absorption Energies of T_1 at Low and High Magnetic Fields

At high magnetic fields $B \geq 11$ T, in Fig. 3*B* of the main text, the LL transition T_1 is shown to split into four submodes due to the Zeeman splitting of LLs. According to the theoretical calculations displayed in figure 3 of the Supplemental Material of ref. 40, the energies of the split T_1 submodes, are defined by the onsets of the absorption features. The definition of the submode energies in the $ZrTe_5$ flake is consistent with that in the material with 3D massless fermions—HgCdTe (see figure 4 of ref. 42). However, when the magnetic field becomes low enough, the split submodes merge and cannot be well distinguished, so at $B \leq 4$ T, only one absorption feature can be observed. At low magnetic fields $B \leq 4$ T, the absorption energies of T_1 of the $ZrTe_5$ flake are defined by the minimal positions of the dip features, which is a standard method for film systems, such as graphene (44). In this supplementary section, we want to check whether the definition of the T_1 energy at magnetic fields $B \leq 4$ T is valid for the $ZrTe_5$ flake.

The close-up image of Fig. S5*A* shows a royal blue dashed curve for fitting the low-field minimal positions of T_1 in Fig. 2 of the main text (with the Fermi velocity $v_F^{T_1} = 4.76 \times 10^5$ m s^{-1} and the bandgap $\Delta = 10$ meV) and a green dashed curve that represents the average energy of the four olive dashed curves for fitting the energies of the four submodes at high magnetic fields. The energy difference between the royal blue and green dashed curves at $B =$ 4 T is at most 2 meV, which is not larger than the energy error bar of the obtained bandgap. We further plotted the minimal positions of T_1 (royal blue dots) at $B \leq 4$ T in Fig. S5*B*. At $B \leq 2$ T, the royal blue dots of T_1 are shown to match well with the four olive dashed curves for fitting the energies of the four submodes at high magnetic fields and the green dashed curve. Thus, although the Landé g factors in thin $ZrTe_5$ flake are large and the splitting of T_1 transition can be well distinguished at high magnetic fields, the consistence between the minimal position of the dip features at $B \leq 4$ T and the fitting curves for the split T_1 modes indicates that defining the minimal position as the absorption energy is a valid method for obtaining the T_1 transition energies at low magnetic fields ($B \leq 4$ T).

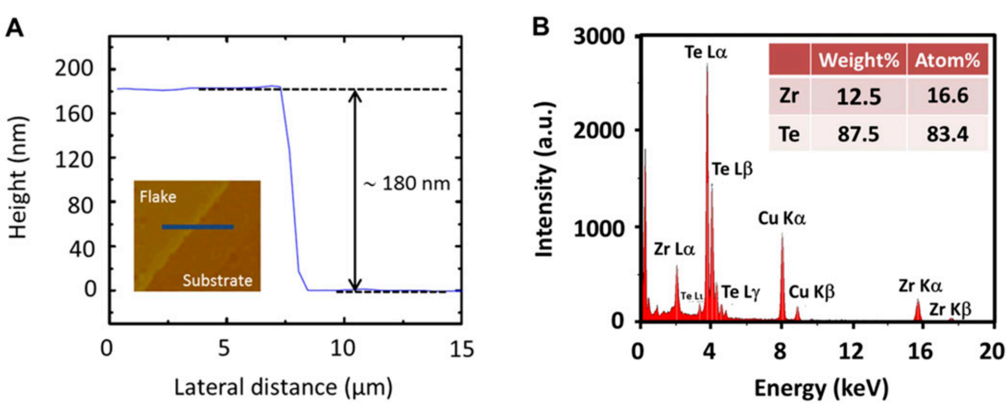

Fig. S1. Basic characteristics of the multilayer $ZrTe_5$ flake. (*A*) Thickness of the $ZrTe_5$ flake characterized by AFM. The multilayer flake studied in the main text has the thickness $d \sim 180$ nm. (*Inset*) An AFM image of the investigated flake. The AFM scan was performed along the blue line in the image. (*B*) Energy dispersive X-ray spectra of the $ZrTe_5$ flake. The atom ratio, Zr:Te ~ 1:5.

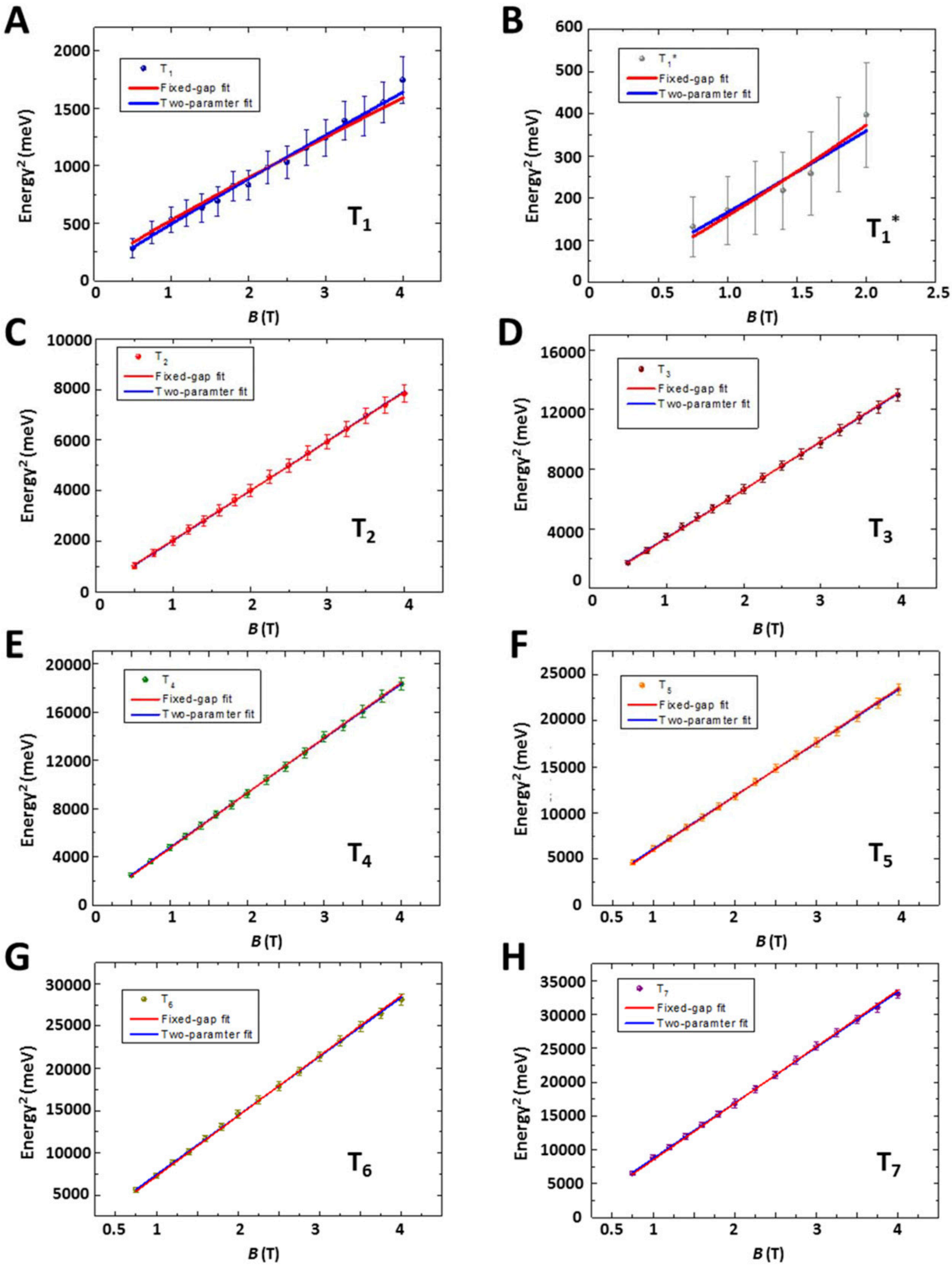

Fig. S2. Least squares fit for the inter- and intra-LL transitions (T_n and T_1*). Squares of T_1 (*A*), T_1*(*B*) and T_n (*C–H*) energies are plotted as a function of magnetic field. Symbols: experimental data. Blue curve: best fit from the first approach. Red curve: best fit from the second approach. For T_n ($7 \geq n \geq 2$), $\chi_1^2 \sim \chi_2^2 \sim 0.999$. For T_1, $\chi_1^2 = 0.988$ and $\chi_2^2 \sim 0.993$. For T_1*, $\chi_1^2 \sim \chi_2^2 \sim 0.940$.

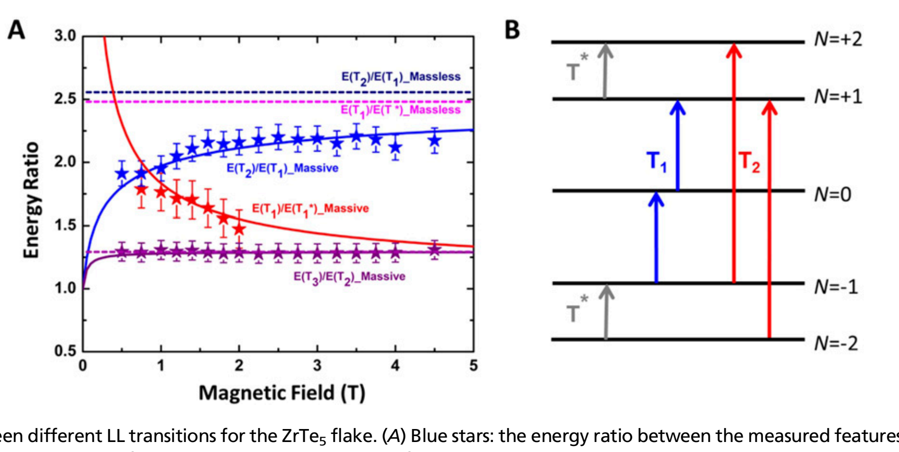

Fig. S3. Energy ratios between different LL transitions for the $ZrTe_5$ flake. (*A*) Blue stars: the energy ratio between the measured features T_2 and T_1. Blue solid line: theoretical result of E_{T2}/E_{T1} based on Eq. 2 of the main text with a bandgap of 10 meV. Red stars: the energy ratio between the measured features T_1 and T_1*. Red solid line: theoretical result of E_{T1}/E_{T1*} based on Eqs. **2** and **3** of the main text with a bandgap of 10 meV. Purple star: the energy ratio between the measured features T_3 and T_2. Purple solid line: theoretical result of E_{T3}/E_{T2} based on Eq. **2** of the main text with a bandgap of 10 meV. Navy dashed line: theoretical result of E_{T2}/E_{T1} based on Eq. **2** of the main text without a bandgap. Magenta dashed line: theoretical energy ratio between the inter-LL transition from LL_0 to LL_{+1} (or from LL_{-1} to LL_0) and the intra-LL transition T* from LL_{+1} to LL_{+2} (or from LL_{-2} to LL_{-1}) based on Eqs. **2** and **3** of the main text without a bandgap. Purple dashed line: theoretical result of E_{T3}/E_{T2} based on Eq. **2** of the main text without a bandgap. (*B*) Schematic of the assumed LL transitions without a bandgap.

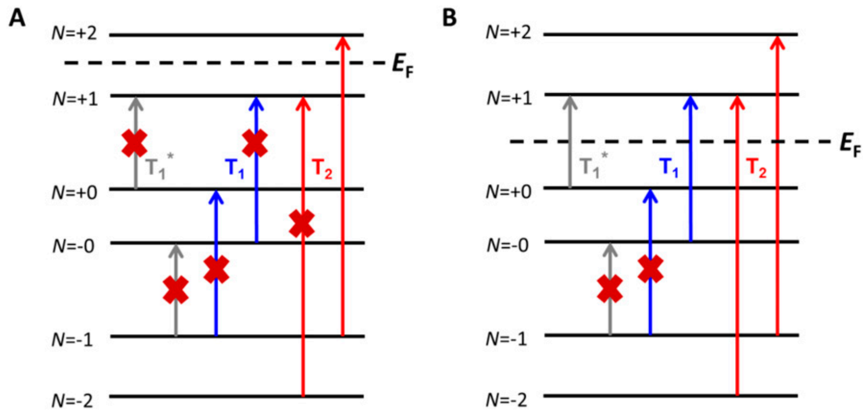

Fig. S4. Schematic of the Landau level transitions at low magnetic fields. (*A*) LL transitions with E_F located between LL_{+1} and LL_{+2}. Both T_1 and T_1* are blocked due to Pauli's exclusion principle. (*B*) LL transitions with E_F located between LL_{+0} and LL_{+1}. The T_1 transition from LL_{-0} to LL_{+1} and the T_1* transition from LL_{+0} to LL_{+1} take place, and the LL transitions, $LL_{-1} \rightarrow LL_{+0}$ and $LL_{-1} \rightarrow LL_{-0}$, are forbidden.

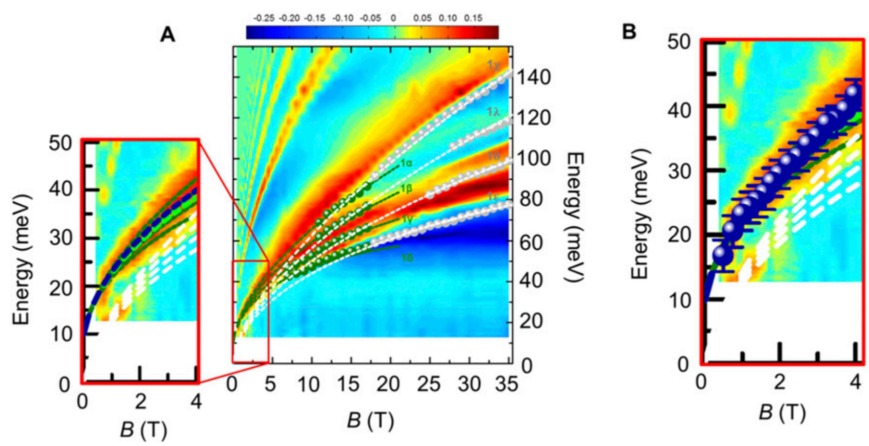

Fig. S5. Comparison of the two ways for defining the T_1 transition energy. (*A*) Split T_1 mode energies as a function of *B* and four olive dashed curves for fitting the inter-LL transitions T_1. The close-up image shows a royal blue dashed curve for fitting the low-field minimal position of T_1 and a green dashed curve representing the average energy of the four olive dashed lines. (*B*) Minimal positions of the dip features T_1 (royal blue dots) at $B \leq 4$ T.

Table S1. Effective Fermi velocities of different LL transitions obtained by the two methods

LL transition	Fermi velocity (method 1) (m/s)	Fermi velocity (method 2) (m/s)
T_2	5.06×10^5	5.04×10^5
T_3	4.97×10^5	5.00×10^5
T_4	4.97×10^5	5.00×10^5
T_5	4.94×10^5	4.98×10^5
T_6	4.92×10^5	4.97×10^5
T_7	4.90×10^5	4.95×10^5
T_1^*	4.07×10^5	4.63×10^5

Method 1: both Δ and v_F are free parameters. Method 2: the gap value is fixed, $\Delta \sim 10 \pm 2$ meV and v_F is a free parameter.